Development of a calibration methodology for fitting the response of a lithium-ion cell P2D model using real driving cycles

Antonio García [*], Javier Monsalve-Serrano, Alberto Ponce-Mora, Álvaro Fogué-Robles

CMT - Motores Térmicos, Universitat Politècnica de València, Camino de Vera s/n, 46022, Valencia, Spain

A B S T R A C T

Pseudo-two-dimensional models based on physical processes are of significant relevance in this field, especially now that computational cost is getting more affordable with new technological advancements. Their biggest demerit is the difficulty in selecting a reduced number of parameters to consider during the optimization process to maintain the coherence of the physical processes and a good compromise in complexity. The current work proposes a methodology in which a selection of 14 critical constructive and performance parameters are iteratively fitted with an affordable computing cost using a genetic algorithm. The objective is to represent with high fidelity the experimental response of real 18,650 lithium-ion cells based on different cathode chemistries (NMC 811 and NCA). The results show that the proposed methodology can deliver better results if the calibration process is performed with a single dynamic driving cycle test instead of a series of constant C-rate curves, maintaining high reliability when simulating dynamic conditions such as driving cycles representative of real transport applications. The maximum voltage Root Mean Square Error (RMSE) of the validation profiles is not exceeding 0.0315 V and 0.0357 V for the NMC 811 and NCA cells, respectively.

1. Introduction

Nowadays, in the context of the energy crisis and environmental pollution, the automotive sector has put conventional powertrains based on internal combustion engines in a tight spot with ever-increasing restrictions on emissions and higher demands in terms of fuel savings [1]. This urgent pursuit of the decarbonization of the automotive sector has brought to light alternative power sources and technologies. Zero-carbon fuels for ICEs [2] and fuel cells [3], like hydrogen or ammonia [4], and hybridization of vehicles [5] are different research lines being considered by the manufacturers. However, a clear trend shows that the preferred alternative is the electrification of the powertrain. In the past five years, hybrid and fully electric vehicles have increased their sales volume by almost 10%, showing their relevance in the present situation [6].

Electric vehicles have clear benefits regarding pollutants emissions savings and noise levels [7], but the capacities of electric batteries currently limit this technology. The autonomy and life expectancy of this component make it very clear that the maturity of this technology is still not on par with previous combustion-based platforms [8]. A considerable effort is being made to improve the performance, energy capacity,

and safety specifications of lithium-ion cells, researching different chemistries for anodes and cathodes, form factors, and packaging of the cells to minimize the impact of weight and volume [9,10]. Due to this, a great variety of alternatives can be found in the market in terms of geometries, being the most common the cylindrical, prismatic, and pouch cells, each of them with different size and capacity options and also different chemistries [11]. Among them, the most used cathode chemistries in transport applications are NCM (Lithium Nickel–Cobalt–Manganese oxide), LFP (Lithium–Iron-Phosphate oxide), NCA (Lithium Nickel–Cobalt–Aluminum oxide), and LCO (Lithium Cobalt Oxide), each of them with different characteristic properties [9,12].

During the design process, when defining battery size, the number of cells, or the vehicle range, numerical models have become an essential tool used for most decisions [13,14]. For this reason, predictive tools capable of accurately predicting the performance of the components are necessary. Battery system models usually depend on single-cell models distributed in series or parallel to scale up the setup [10]. Single-cell performance can be easily measured with limited instrumentation, and a wide scope of testing conditions will significantly improve the dataset's quality. However, these datasets are fed to a battery cell model that has to be able to capture all the main performance indicators of the

---

* Corresponding author.
  E-mail address: angarma8@mot.upv.es (A. García).

cell, like the heat production and drop in capacity at high power output, how working temperatures affect the voltage output, or other effects like the degradation over time depending on the purpose of the model [15]. As can be seen, the features that an all-purpose battery cell model should have, are mainly to capture voltage output and temperature dependencies of other parameters while accommodating any cell chemistry and geometry or size.

The most commonly used models in current applications are those based on the equivalent circuit model (ECM), which are simple and easily scaled in complexity by adding branches of resistance-capacitor (also referred to as RC branches) to represent experimental data [14, 15]. The main limitation of these models is that they do not consider physical phenomena and changes occurring inside the cell driven by the electrochemical reaction. Hence, they require extensive experimental datasets to accommodate temperature or aging effects. Thus, the reliability while predicting the state of charge (SOC) [16,17] or state of health (SOH) is always limited [18], even with the use of advanced techniques and neural networks [19]. As an alternative, pseudo-two-dimensional electrochemical models based on Newman et al. [17] work provide a set of equations capable of replicating the physicochemical and electrochemical evolution within the cell components, including thermal behavior and aging processes in the prediction capabilities of the model [20]. The complexity of solving these equations has now become affordable for the onboard systems equipped in the vehicles, but these models require a detailed definition of the tuning parameters to make them reliable over time. Additionally, this type of electrochemical models can be coupled with other sub-models to include evaluations on the mechanical and thermal behavior of the cell during cycling aging or under very demanding conditions that may induce failure modes like thermal runaway [21,22]. By considering these extreme cases the tools can be applied to evaluate and design auxiliary systems of the battery like the cooling system and ensure their functionality [23].

The available parameters to optimize in the Doyle-Fuller-Newman (DFN) model include external geometric values that can be readily fixed once the cell model is known and many internal physical and electrochemical variables difficult to define without disassembling the element [24,25]. The definition of these unknown variables by fitting performance curves has become a research topic to address, and few works can be found discussing which variables should be optimized and which method should be applied to find the optimum value in order to define a common methodology to follow. Different optimization methods have been evaluated in the literature, including techniques like Gauss-Newton (GN) method [26], Levenberg-Marquardt (LM) method [27], Bayesian framework [28], Particle Swarm Optimization (PSO) [29] or Genetic Algorithms (GA) [30,31]. Stochastic optimization algorithms like PSO or GA have shown better performance to fit the experimental data with the drawback of increased computational cost. However, the most relevant aspect while capturing the cell's electrochemical response is identifying the most relevant parameters to include in the optimization [32]. For basic performance data at a constant current level (C-rate), some authors have identified that for low power outputs and restricted dynamic behavior, a reduced number of variables would be capable of replicating the experimental results with good precision [29,33,34]. As the model's validity range is widened by including the effects of higher output levels and the ambient temperature, as well as the thermal evolution of the cell, the required parameters to include in the optimization can vary from 16 to 88 [30,31,35,36].

As can be observed, depending on the data used for the calibration (steady operation, low or high output power, dynamic cycles, cell temperature evolution, etc.), the number of parameters to optimize can be overwhelming and unacceptable for the definition of a control system based on the DFN model. Identifying the most relevant parameters within a reduced selection of them and maintaining accuracy on the performance predicted with a methodology capable of adapting to different cell geometries and chemistries is of interest in developing future electric systems.

The main objective of the current research is to propose a novel calibration and validation methodology for a lithium-ion cell P2D model. The fitting process uses experimental datasets consisting of stationary performance curves at several constant C-rates, as well as dynamic high-rate driving cycles representative of realistic driving. The secondary objective is to verify that the fitting procedure can be carried out precisely with a limited set of optimization variables and to assess if the method maintains its validity with different cathode chemistries.

The one-step fitting process of a P2D model described in the present research is characterized by singular, innovative aspects. Firstly, the sophisticated battery model is fitted to experimental results with a reduced number of parameters (optimization variables), reduced usage of experimental tests, and an acceptable computing cost. The parameter selection is conducted iteratively, fitting key constructive and operational parameters frequently unknown or subject to variability among cell specimens. The fitting of the cell response accounts simultaneously for the thermal and the electrical response of the cell, and the methodology has prioritized making a reliable prediction of the cell response under realistic driving cycles, which is a challenging scenario relevant in the automotive context.

Lastly, all the process is carried out using a commercial code, which allows the model scalability and ease of integration with full-vehicle models and, at the same time, facilitates the reproducibility of the study. All the numerical work consisting of calibrating and validating the computational model is performed using the commercial software GT-AutoLion within the GT-Power platform from Gamma Technologies [37].

2. Description of the computational model

All the numerical simulations included in this work have been performed using the GT-Suite platform from Gamma Technologies. Their GT-AutoLion package provides a complete and versatile set of models and sub-models prepared for lithium-ion battery cell simulation. Constant current, constant voltage, or dynamic cycle simulations are all well within the capabilities of the numerical platform. The basis of this package is the pseudo-2D physicochemical model initially developed by Doyle, Fuller, and Newman for predicting battery performance from the estimation of the reaction rate in which lithium ions and electrons are transferred from cathode to anode, considering resistance growth and temperature changes during the battery operation. The model is accompanied by a database of material properties that covers most of the commercially available chemistries in the market for cathode, anode, electrolyte, or separator, but it is also possible to modify these properties to accommodate the user's needs. On top of this electrochemical model, a series of degradation mechanisms are included to account for battery aging, like solid electrolyte interface growth or lithium plating, among many others. Also, other sub-models, like double-layer capacitance model for a detailed analysis of capacity losses [38], or a mechano-electrochemical model for strain prediction from active material swelling based on lithium intercalation and thermal expansion of the materials [21] are available for more detailed and specific studies. These sub-models are very useful for very specific applications or studies, like aging effects, second life applications or very specific applications where the other electronic components have a direct effect on the battery performance. Given the complexity of these models, the amount of data needed to adequately fit their behavior, and the limited relevance they have under normal operation conditions of the cells, they have been neglected in the present study.

For this reason, the present approach focuses on the basic electrochemical model under non-extreme operating conditions. It neglects aging effects to understand better how this calibration procedure should be applied.

The DFN model is based on the porous electrode theory developed by Newman et al. [39], in which electrodes are conceptualized as solid
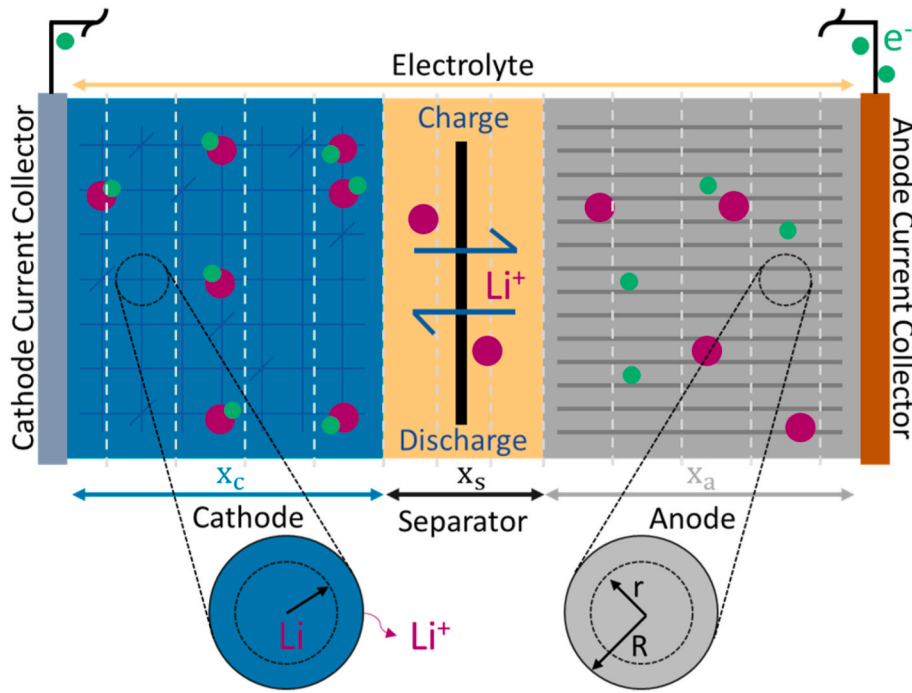
Fig. 1. Conceptual sketch of the pseudo-two-dimensional electrochemical model.

solution particles on the microscopic scale for which species intercalation is modeled based on a surface of exchange and a concentration difference. To this approach is then added a longitudinal scale to account for species transport in the macroscopic scale in the electrode and from one electrode to another through the separator, which will create the potential difference between both electrodes and define the current. A general sketch of the conceptualized P2D model can be found in Fig. 1, showing the longitudinal disposition of the anode and cathode solid phases submerged in the electrolyte, each modeled as a series of particles that adsorb and deliver lithium ions and electrons.

The essence of the electrochemical model is defined through a set of ordinary differential equations (ODEs). Particularly, mass balance and species conservation have two governing equations, one in the particles' radial direction and one for through-plane macroscopic transport. Charge conservation adds another two ODEs for the solid phase and electrolyte, respectively, both in the macro scale. The Butler-Volmer equation that defines lithium intercalation reaction rates is then utilized to give closure to this ODE system. Because the physicochemical properties of the materials are highly dependent on the working temperature of the cell, the temperature evolution requires an additional governing equation for thermal balance, in which the thermal behavior of the cell assumes a lumped mass with different heat sources (electrochemical reactions, internal resistance, and entropic heat generation) and heat transfer boundaries (convective heat transfer to the ambient or conductive heat transfer to a cooling system for example). The most relevant aspects of this ODE system are described in more detail in the following subsections.

2.1. Species conservation in the electrolyte and active materials

As a general notion, during the redox reactions that take place during the operation of a lithium-ion battery cell, a few species appear and disappear and are then transported from the anode to the cathode through the electrolyte [40]. Lithium stored in the active material is separated into lithium ions that travel through the electrolyte and the separator and electrons that create an electric current that travels through the external circuit. Therefore, lithium ions can be considered to only appear on the electrolyte while moving between electrodes. The longitudinal transport of lithium ions is governed by Eq. (1), considering the porous medium and potential difference:

$$\frac{\partial}{\partial_x}[\varepsilon c_e] = \frac{\partial}{\partial_x}\left(D_e^{eff}\frac{\partial c_e}{\partial x}\right) + \frac{1 - t_+^0}{F}j^{Li} \qquad (1)$$

Where ε is the porosity, c_e is the molar concentration of lithium ions in the electrolyte, D_e^{eff} denotes the electrolyte effective diffusion coefficient, F is Faraday's constant, t_+^0 is the transference number, and j^{Li} is the reaction current of lithium.

It is worth mentioning that whenever a diffusion coefficient, ionic conductivity, or other transfer parameters are referred to as effective, they are accounting for porosity effects through the Bruggeman relation [41], in which a transport property (A) has an effective value scaled with the porosity of the medium (ε) and the Bruggeman tortuosity exponent (p) as defined by Eq. (2):

$$A^{eff} = A\varepsilon^p \qquad (2)$$

The values of these exponents have been studied by other authors, and a widely accepted hypothesis assumes a value of $p = 1.5$ for mass, thermal, electric, and ionic conductivities [42,43].

Once the lithium ions reach the solid electrodes, a reaction to turn them into lithium and an intercalation process occur at the microscale. Based on Fick's law of mass diffusion and Ohm's law for electrical potential distributions, the concentration of lithium in the radial direction of the particles in the active materials c_s can be described by Eq. (3):

$$\frac{\partial c_s}{\partial_x} = \frac{1}{r^2}\frac{\partial}{\partial_x}\left(D_s r^2 \frac{\partial c_s}{\partial r}\right) \qquad (3)$$

Being r the radius of the particle and D_s the diffusion coefficient of lithium in the solid phase.

2.2. Charge conservation in the solid and electrolyte phases

The involvement of potential differences in the transport of species and the current generation also demands considering charge transport in the equations. Also, different formulations should be applied given the different nature of charge transport through the liquid electrolyte and

through the solid phases of active material. In the DFN model, the derivation of the main equations is based on the hypothesis of electro-neutrality, which defines that, as stated by Newman, *"a volume element within the porous electrode will be, in essence, electrically neutral because it requires a large electric force to create an appreciable separation of charge over an appreciable distance"* [39,40,44].

In the case of solid phases, the electrons are transmitted mainly by electric conductivity, so the reaction current can be defined by the formula in Eq. (4):

$$0 = \frac{\partial}{\partial_x}\left(\sigma_s^{eff}\frac{\partial \varphi_s}{\partial x}\right) - j^{Li} - a_{dl}C\frac{\partial(\varphi_s - \varphi_e)}{\partial x} \tag{4}$$

where σ_s^{eff} is the effective solid-phase conductivity, φ_s is the solid phase potential and j^{Li} is the reaction current of lithium. The additional term refers to double-layer capacitance, considering φ_e as the liquid phase potential, a_{dl} as the specific interfacial area and C as the specific capacitance.

In the case of the electrolyte, current flow occurs mainly through ionic conductivity and diffusional conductivity. The presence of electrons and lithium ions in the electrolyte can lead to the formation of metallic lithium, considered one of the main degradation mechanisms in the literature, but in this case, such a source of lithium losses is not considered. With this assumption, the electric potential through the electrolyte is expressed as in Eq. 5

$$0 = \frac{\partial}{\partial_x}\left(k^{eff}\frac{\partial \varphi_e}{\partial x}\right) + \frac{\partial}{\partial_x}\left(k_D^{eff}\frac{\partial lnc_e}{\partial x}\right) + j^{Li} + a_{dl}C\frac{\partial(\varphi_s - \varphi_e)}{\partial x} \tag{5}$$

where k^{eff} is the electrolyte's effective ionic conductivity, and c_e the Li$^+$ concentration in the electrolyte. The parameter k_D^{eff} is the ionic diffusional conductivity that can be obtained by Eq. (6):

$$k_D^{eff} = \frac{2R^0Tk^{eff}}{F}(t_+^0 - 1)\left(1 + \frac{dlnf_\pm}{dlnc_e}\right) \tag{6}$$

with R^0 is the gas constant, T corresponds to the temperature, and F is Faraday's constant, t_+^0 is the transference number and $f_\pm$ is the molar activity coefficient in the electrolyte [45,46].

To relate all four main ODEs described for species and charge conservation, the Butler-Volmer equation represented in Eq. (7) defines how the electrical current through an electrode depends on the voltage difference between the electrode and the bulk electrolyte. The equation is derived considering the charge neutrality principle of an electrode-electrolyte interface and governs the net charge production rate by summing the forward rate of current production and the backward rate of current production [47].

$$j^{IC} = a_si_0\left[e^{\frac{a_aF}{R_uT}\left(\eta - \frac{R_{SEI}j^{Li}}{a_s}\right)} - e^{-\frac{a_cF}{R_uT}\left(\eta - \frac{R_{SEI}j^{Li}}{a_s}\right)}\right] \tag{7}$$

In this equation, a_s is the volume-specific reaction surface area, i_0 is the exchange current density, α is the charge transfer coefficient, R_u is the universal gas constant and R_{SEI} is the resistive film layer. The overpotential, η, can be defined as the difference between the solid (φ_s) and liquid (φ_e) phases potentials, minus the open-circuit potential of the solid (U):

$$\eta = \varphi_s - \varphi_e - U \tag{8}$$

One of the main concerns of this equation is the symmetry between the charge transfer coefficient for the anode (α_a) and cathode (α_c). Some studies show that under extreme temperature conditions, non-symmetric behavior can be observed [48]; nonetheless, the most common hypothesis is that both parameters take the value of 0.5 [47,49]. Since no extreme conditions are included in this study, this last hypothesis will be maintained for simplicity.

2.3. Theoretical capacity and stoichiometry for a battery cell

During the battery operation, not all the Li content within the active material can be cycled. In this sense, the theoretical capacity $C_{s,max}$ may not be the best parameter to represent the working capacity of the battery cell. Conventionally, the maximum useable capacity of a cell is defined by its first discharge capacity. In addition, other parameters, such as the ratio between the mass-specific first charge capacity (q_{fcc}^{cat}) and mass-specific first discharge capacity (q_{fdc}^{cat}) divided by their mass-specific theoretical capacity (q_{th}^{cat}) can be used to express how the cell deviates from its maximum capacity, as shown in Eq. (9) and Eq. (10).

$$\gamma_{fcc}^{cat} = \frac{q_{fcc}^{cat}}{q_{th}^{cat}} \tag{9}$$

$$\gamma_{fdc}^{cat} = \frac{q_{fdc}^{cat}}{q_{th}^{cat}} \tag{10}$$

Where γ is the ratio of first discharge and first charge capacity. Therefore, the cathode stoichiometry can be defined as presented in Eq. (11):

$$Stoichimetry = \frac{C_s}{C_{s,max}} \tag{11}$$

2.4. Thermal balance of the cell

For the temperature evolution of the cell, an additional differential equation is included governing the energy balance over a zero-dimensional thermal mass in which heat transfer to the ambient and heat generation from the electrochemical model are accounted for as per Eq. (12). Heat transfer to the ambient is simplified to convective heat transfer to the ambient temperature only since no cooling system or external thermal management system are included in the study. A realistic prediction of the cell temperature is essential since it will affect the transfer properties of the materials.

$$\rho c_p \frac{dT}{dt} = \dot{q}_{gen} + \dot{q}_{conv} \tag{12}$$

$$\dot{q}_{conv} = \frac{hA_c(T - T_{amb})}{V_c} \tag{13}$$

The heat sources during the cell operation include several mechanisms, to say, the heat generated during the redox reactions ($\dot{q}_{rxn}$), the reversible heat generated during intercalation and de-intercalation processes coming from lithium movements ($\dot{q}_{rev}$), the ohmic heat due to electronic and ionic flows within the cell ($\dot{q}_{ohm}$), and the heat generated due to contact resistance at the current collectors ($\dot{q}_c$). Irreversible entropic heat generation can be accounted for within the term ($\frac{\partial U}{\partial T}$), that denotes the changes of the open circuit potential with temperature. Eq. (14)–(18) show the definition of each of these terms following Bernardi's model [50,51].

$$\dot{q}_{gen} = \dot{q}_{rxn} + \dot{q}_{rev} + \dot{q}_{ohm} + \dot{q}_c \tag{14}$$

$$\dot{q}_{rxn} = \frac{1}{L}\int_0^L j^{Li}\eta \, dx \tag{15}$$

$$\dot{q}_{rev} = \frac{1}{L}\int_0^L j^{Li}\left(T\frac{\partial U}{\partial T}\right) dx \tag{16}$$

$$\dot{q}_{ohm} = \frac{1}{L}\int_0^L \left[\sigma^{eff}\left(\frac{\partial \varphi_s}{\partial x}\right)^2 + \kappa^{eff}\left(\frac{\partial \varphi_e}{\partial x}\right)^2 + \kappa_D^{eff}\left(\frac{\partial ln\, c_e}{\partial x}\right)\left(\frac{\partial \varphi_e}{\partial x}\right)\right] dx \tag{17}$$

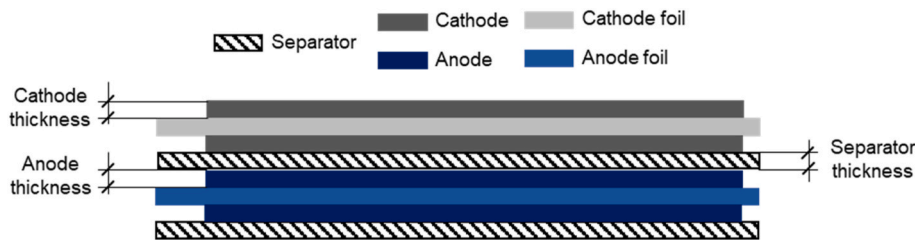$$\dot{q}_c = \frac{R_c}{A_sV_c}I^2 \tag{18}$$

Fig. 2. The layered structure of the lithium-ion cells subject to analysis.

3. Description of the fitting methodology

3.1. Description of the experimental datasets

The experimental data used to fit the electrochemical models come from a characterization campaign carried out on two lithium-ion cells with a 18,650 format. Researchers of McMaster University published the first dataset, including discharges at a constant C-rate, OCV discharges, Hybrid Power Pulse Characterization (HPPC), and drive cycles (US06, HWFET, UDDS, and LA92) for different ambient temperatures. The sample subject to the characterization campaign is an LG Chem INR18650HG2 (NMC 811) [52].

To verify the successful extension of the methodology to other cathode chemistries, the calibration and validation processes defined have been reproduced with a Panasonic 18650 PF 2.9 Ah cell (NCA), tested by the same authors following the same standards at the University of Wisconsin-Madison [53].

The curves used to calibrate the cell are the voltage and temperature response under constant or variable current demands in both charging and discharging for an ambient temperature of 25 °C. A reduced number of experimental tests for calibration have been employed, seeking to simplify the fitting procedure while maintaining an affordable computing cost. The cell undergoes a complete discharge in the curves used for calibration and validation.

3.2. Definition of the manipulable variables

This section specifies the parameters manipulated by the genetic algorithm during the optimization process. Usually, cell manufacturers do not provide these technical specifications and are a priori unknown to end-users. Notwithstanding, their correct definition is crucial to representing the cell response and obtaining a predictive electrochemical model. Other works in the literature address the problem of parameter set identification in an iterative process, reducing an extensive set to only the most relevant ones. Other methods, like applying intrusive or destructive tests and measurements, can contribute to the model accuracy by actually obtaining the real value of some constructive and operative parameters. From these works, some guidelines can be extracted.

One of the most elementary parts to be defined in the mode is determining the total amount of materials (anode, cathode, separator, and electrolyte). According to Forman et al. [30] in which they optimized a total of 88 parameters, they identified the definition of total material as the most relevant set of parameters. These depend on a multitude of parameters and factors like assembly technology, and they can be defined in the model in a series of totally equivalent manners, like using volumetric fractions [34], densities, or porosities [31]. Using the extensive material properties database included in the Gamma Technologies platform, the densities remain as defined by the database, and the parameters to modify are layer thickness and particle size. To define the total amount of lithium, one can find the actual maximum and minimum concentrations for anode and cathode as done by Chu et al. [35] in their work, where they included a total of 28 parameters in their optimization, but in this case, the first charge and discharge specific

capacities for anode and cathode, as well as their total capacity, will serve the same purpose. The rest of the parameters, like volumetric fractions or porosities, can be related and computed to these constructive and loading parameters. In the work of Zhang et al. [31], in which a total of 27 parameters were considered to characterize a cell behavior, they highlighted the relevance of the complete cell's thermal characterization and heat transfer to the ambient. For the lumped mass approach, the mass-specific heat capacity and the convective heat transfer coefficient are all the required parameters to tune. For the heat sources, the contact resistance was identified to be most relevant in the same work.

Considering the literature on parameter identification, the most relevant parameters have been selected for the current study, forming a parameter set of 14 variables to consider in the optimization. The constructive characteristics and electrochemical design attributes subject to fitting are listed below:

- Cathode (t_{cat}), anode (t_{an}), and separator (t_{sep}) thicknesses [µm].
- Particle size of the anode (R_{an}) and cathode (R_{cat}) active material [µm].
- First charge capacity of anode (q_{fcc}^{an}) and cathode (q_{fcc}^{cat}) [mAh/g].
- First discharge capacity of anode (q_{fdc}^{cat}) and cathode (q_{fdc}^{cat}) [mAh/g].
- Anode (C_{an}) and cathode (C_{cat}) capacity [Ah].
- Specific heat capacity (c_p) of the cell [J/(kg·K)].
- Convective heat transfer coefficient (h) [W/(m^2·K)].
- Contact Resistance (R_c) [Ω·m^2].

The final selection of parameters includes constructive elements, like the thickness of each material layer that composes the cell, which may show a significant deviation from cell to cell due to the manufacturing process [54]. The constructive characteristics can be identified in Fig. 2. The total charge capacity of the cell is considered through a series of parameters that define the lithium inventory available and the capacity of each electrode to allocate the lithium. Finally, thermal effects have been modeled through the convective heat transfer and heat capacity, as well as other variables intimately related to heat generation, like contact resistance. All the previous variables interact in a complex manner to define the overall cell behavior.

The genetic algorithm iteratively modifies the value of the 14 input variables within prescribed bounds to minimize the objective function. The first selection of variables (initial guess of parameters for the first design) of the optimization process corresponds to default database conditions given by the software, which are at least a coherent starting point. GT AutoLion has an embedded database containing reasonable estimations of cell parameters for different cathode and anode chemistries and expressions governing their temperature dependence.

Those cell parameters that do not participate in the optimization process keep the same database default value throughout the fitting process.

3.3. Non-manipulable inputs for the computational model

The main non-manipulable inputs for the computational simulation are the experimental tests' current, temperature, and voltage profiles.
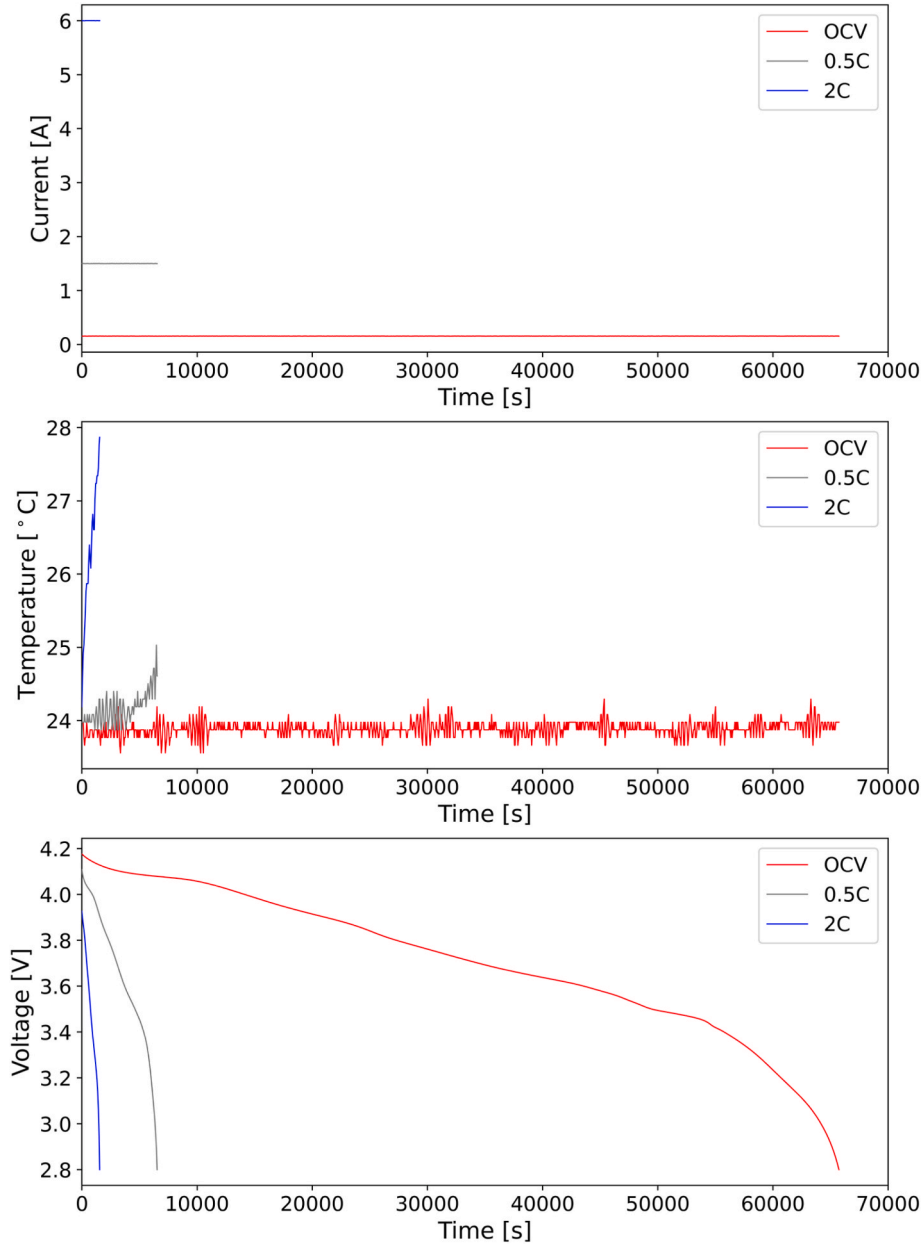
Fig. 3. Current, temperature, and voltage constant C-rate curves for the cell LG Chem INR18650HG2.

Two different tests have been used for the calibration process: constant C-rate discharge profiles (see Fig. 3) and dynamic currents of different magnitudes and signs. The latter profiles are applied in a way that represents a driving cycle (see Fig. 4). The rationale for using the constant C-rate curves for calibrating is that the manufacturers usually provide this data, so it is frequently available for the end-users. The dynamic tests are, in contrast, less accessible to end-users. In the validation stage, the model is fed exclusively with dynamic profiles.

As illustrated in the calibration profiles shown in Figs. 3 and 4, at the end of the test, the cell is close to its lower cutoff voltage.

3.4. Performance indicators and objective function for the calibration process

The objective function of the optimization procedure is the minimization of the voltage and temperature error between the simulated curves and the actual response when a specific current profile is applied to the cell. The objective function is expressed mathematically in Eq. (19):

$$E_{ov} = \frac{1}{n} \sum_{k=1}^{n} \left(w_V \cdot \frac{E_V^k}{f_V} + w_T \cdot \frac{E_T^k}{f_T} \right) \tag{19}$$

$$E_V^k = \sqrt{\frac{\int_{t_{start}^k}^{t_{end}^k} \left(V_{sim}^k(t) - V_{exp}^k(t) \right)^2 dt}{\left(t_{end}^k - t_{start}^k \right)}} \tag{20}$$

$$E_T^k = \sqrt{\frac{\int_{t_{start}^k}^{t_{end}^k} \left(T_{sim}^k(t) - T_{exp}^k(t) \right)^2 dt}{\left(t_{end}^k - t_{start}^k \right)}} \tag{21}$$

Where f_V and f_T are the normalization terms of the voltage and temperature error, respectively. Besides, n is the total number of experimental profiles (signals) used in the calibration process, and the index k refers to each voltage and temperature profile participating in the calibration procedure, and w_V and w_T are the weight factors of the voltage
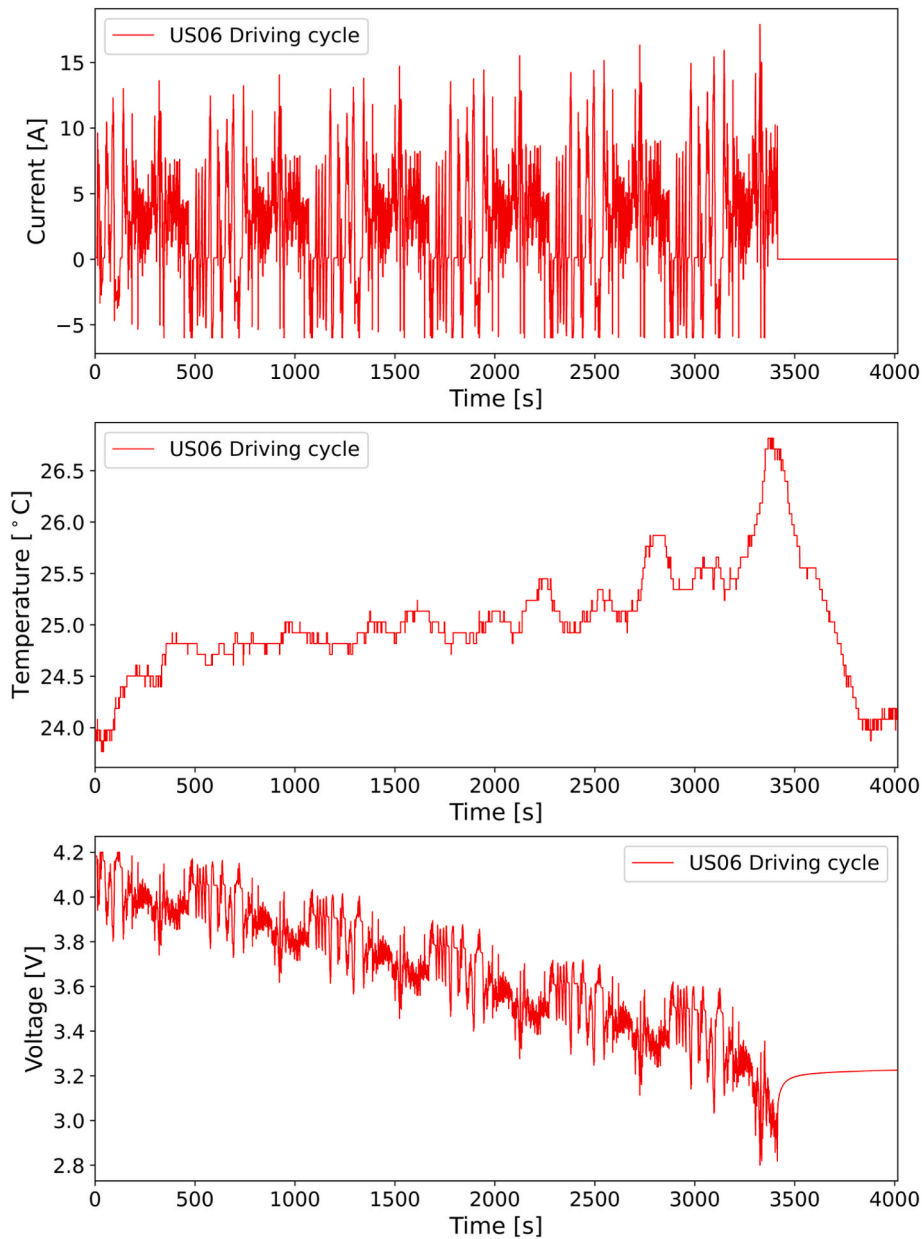
Fig. 4. Current, temperature, and voltage profiles for the cell LG Chem INR18650HG2.

and temperature profiles. The temperature profile is introduced in the optimization process but with a lower weight in the objective function [55]. The weight of the temperature error term has been adjusted iteratively upon analyzing the temperature and voltage discrepancies between experimental and numerical results ($w_T = 0.1 \cdot w_V$).

The underlying principle of the calibration iterative fitting process is depicted in Fig. 5. It shows the workflow to move from the input data to the model setup and optimization process, considering the constraints and fitting indicators used to decide if the optimization process has converged to a successful solution according to the optimization history. The optimization process has been stopped when the rate of change of the overall error (E_{ov}) is close to zero. As will be discussed later, this leads to acceptable $RMSE_V$ values in all the simulations.

Once the best-fitting constructive and electrochemical characteristics have been found, the cell response is evaluated with other cycle profiles different from the one(s) used in the calibration. At this point, the quality of the solution is contrasted with the experimental results by comparing key performance indicators.

3.5. Performance indicators for the validation process

The quality of the fitting in the validation process has been assessed by evaluating key goodness of fit indicators. The precision of the instantaneous response has been mainly assessed by comparing the Root Mean Square Error (RMSE), the 95th percentile error (ΔV_{95th}) and the probability density function of the voltage experimental and simulated profiles.

The analysis has been complemented by comparing the total energy charged (ch) and discharged (dch) during the tests, as expressed in Eq. (22), Eq. (23), Eq. (24), and Eq. (25). The relative error (ε) between the energy charged or discharged in the tests and simulations serves as a proper global goodness of fit indicator:

$$\varepsilon_{ch} = \frac{E_{ch,sim} - E_{ch,exp}}{E_{ch,exp}} \tag{22}$$

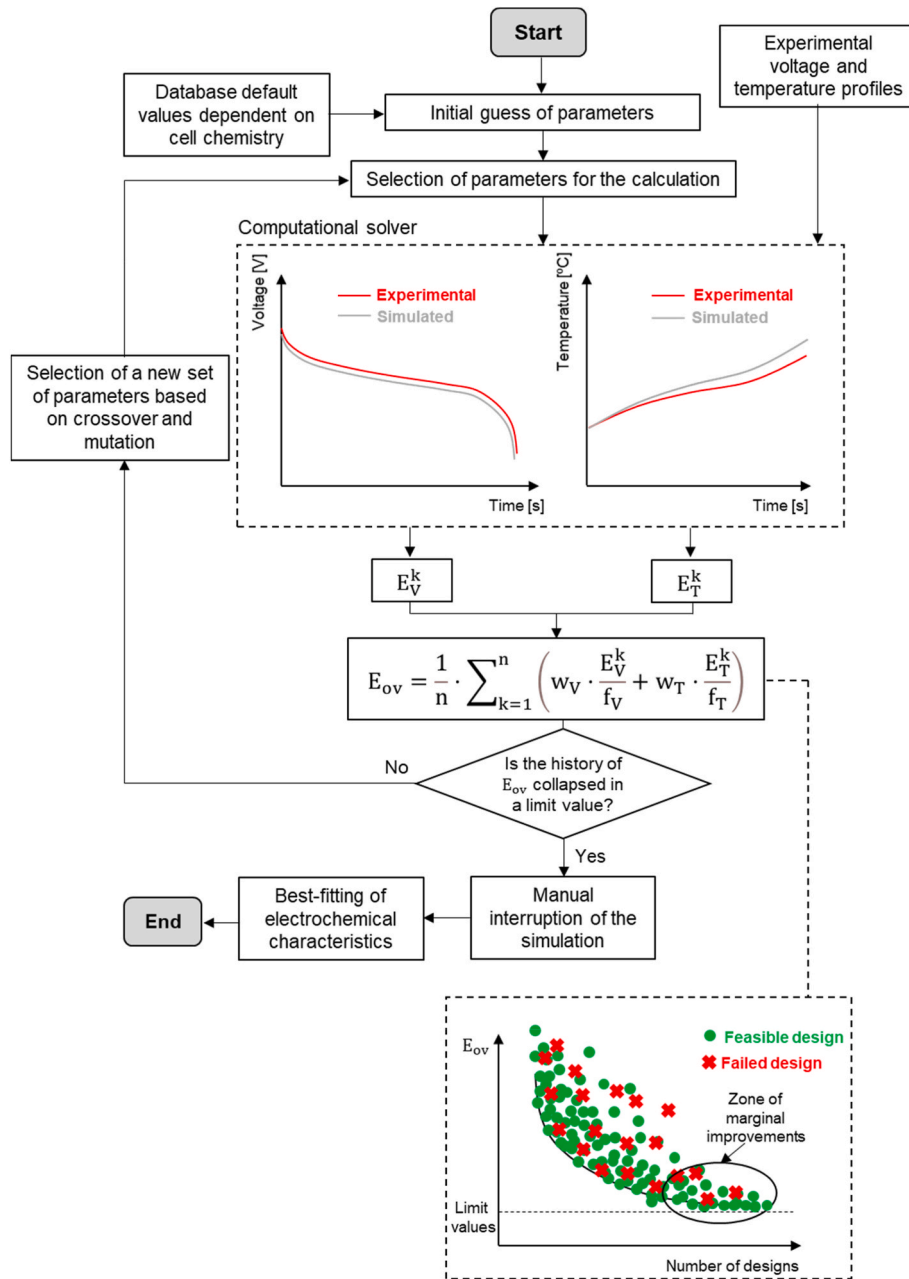$$\varepsilon_{dch} = \frac{E_{dch,sim} - E_{dch,exp}}{E_{dch,exp}} \tag{23}$$

Fig. 5. Flowchart and decision-making of the cell calibration algorithm.

Table 1
Optimum operational and constructive parameters obtained in the calibration procedure of the cell LGHG2 using constant C-rate profiles.

Parameter	Symbol	Units	Value
Cathode thickness	t_{cat}	μm	51.78
Anode thickness	t_{an}	μm	62.84
Separator thickness	t_{sep}	μm	16.63
Cathode first charge capacity	q_{fcc}^{cat}	mAh/g	197.25
Anode first charge capacity	q_{fcc}^{an}	mAh/g	373.02
Cathode first discharge capacity	q_{fdc}^{cat}	mAh/g	179.20
Anode first discharge capacity	q_{fdc}^{an}	mAh/g	355.00
Particle size of the cathode material	R_{cat}	μm	2.79
Particle size of the anode material	R_{an}	μm	14.92
Contact resistance	R_c	$\Omega \cdot m^2$	$3.70 \cdot 10^{-4}$
Anode capacity	C_{an}	Ah	3.19
Cathode capacity	C_{cat}	Ah	3.17

$$E_{ch,sim} = \sum_{i=1}^{n} \int_{t_0^i}^{t_f^i} I_{ch,sim}^i(t) \cdot V_{ch,sim}^i(t) \cdot dt \tag{24}$$

$$E_{dch,sim} = \sum_{i=1}^{n} \int_{t_0^i}^{t_f^i} I_{dch,sim}^i(t) \cdot V_{dch,sim}^i(t) \cdot dt \tag{25}$$

where n is the number of the profile time slots in which charge or discharge currents are applied, being delimited by a change in the current sign.

4. Results

4.1. Calibration based on constant C-rate curves and validation based on dynamic profiles

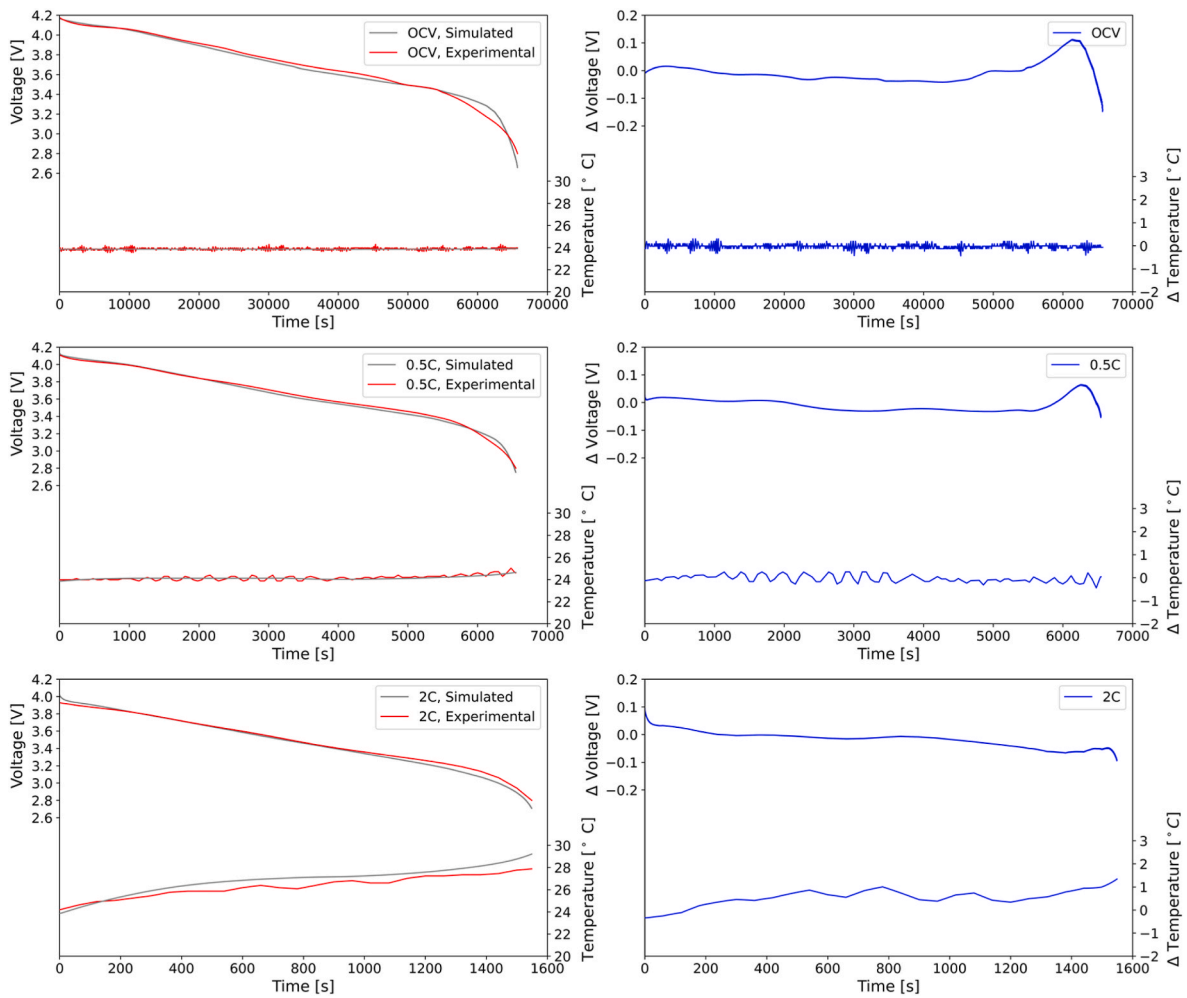Lithium-ion cell manufacturers usually provide the cell response (in

Fig. 6. Voltage and temperature response for the calibration process for constant C-rate curves. Lithium-ion cell: LG Chem INR18650HG2.

terms of temperature and voltage) for several constant currents in the datasheet. In case of satisfactory calibration of the electrochemical model with this data and adequate validation, it would be possible to generate a computational model of the lithium-ion cell with simplified datasets widely available. Table 1 collects the optimum performance and constructive parameters, and Fig. 6 represents the voltage and temperature profiles of the three constant C-rate curves used to calibrate the model (experimental response, simulated response, and the difference between both). The goodness of fit indicators corroborates that the calibrated model reproduces the cell response precisely. For the OCV curve, the discrepancy in the discharge energy corresponds to $\varepsilon_{dch} = -0.21\%$ while the $RSME_V = 0.0367\ V$, and the 95th percentile error for voltage (ΔV_{95th}) equals to 0.088 V, respectively. Fittings with comparable accuracy are observed for the 0.5C ($\varepsilon_{dch,0.5C} = -0.24\%$, $RSME_V = 0.0247\ V$, $\Delta V_{95th} = 0.0377$) and the 2C discharge curves ($\varepsilon_{dch,2C} = -0.49\%$, $RSME_V = 0.0319\ V$, $\Delta V_{95th} = 0.0631\ V$).

Since the temperature increase in the cell during the test is small, and the discrepancies in the temperature profile are below 1.3 °C, it is assumed that the thermal response is well captured, and the voltage goodness of fit indicators have been considered of greater interest.

As can be noticed from the plots on the right side of Fig. 6, the general trend of the modeling error tends to increase as the battery cell is discharged, inducing higher predicting error under low SOC conditions.

Fig. 7 represents the voltage response when the already calibrated cell model is validated with the Mixed-3 dynamic profile. It should be noted that the optimum model settings found in the calibration process have been imposed. The goodness of fit indicators suggest that the cell

dynamic response is predicted with good accuracy when the cell is calibrated with constant C-rate profiles ($\varepsilon_{dch} = -1.21\%$, $RMSE_V = 0.0531\ V$, $\Delta V_{95th} = 0.1107\ V$), however, the error has increased in comparison to the calibration process. The same trend is ratified with the validation profile Mixed-8 ($\varepsilon_{dch} = -0.99\%$, $RSME_V = 0.0463\ V$, $\Delta V_{95th} = 0.1124\ V$). The probability density function of the error distribution (see Fig. 8) demonstrates that the discrepancies in voltage prediction are contained within the interval [−0.1 V, +0.15 V] for both validation profiles. It must be outlined that the probability density function has been normalized so that the total area of the histogram equals 1.

Taking again the previous comment on the error induced in the calibration process, Fig. 7 clearly shows how the committed error in the voltage prediction increases towards the end of the cycle, where the SOC of the cell is approaching complete depletion of the available energy. Also, from Fig. 8, it is possible to observe how there is a voltage peak around +0.1 V in the error distribution curve. This error is present irrespective of the driving cycle and corresponds to the low SOC region.

4.2. Calibration and validation based on dynamic profiles

4.2.1. Cell 1: LG chem INR18650HG2

An alternative methodology in which the calibration method is carried out with dynamic profiles has been proposed to improve the validation results of the previous procedure. Table 2 summarizes the optimum constructive and operational cell parameters obtained after the calibration process. As should be expected, Tables 1 and 2 show
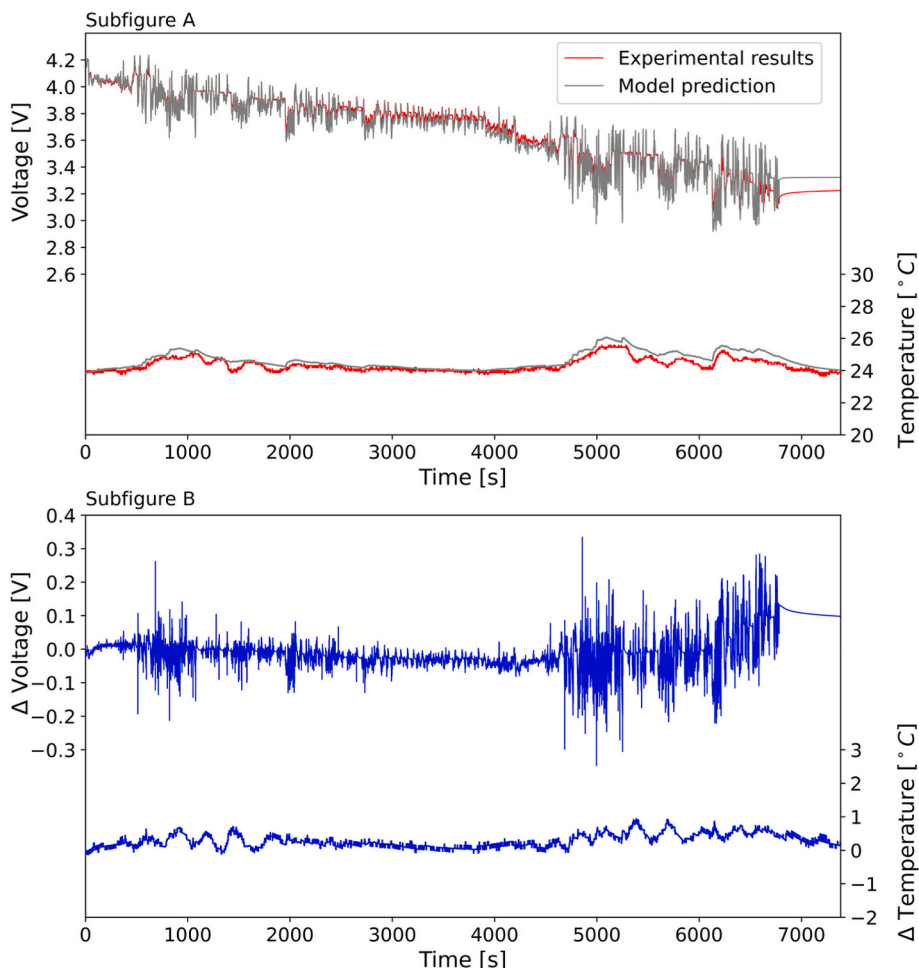
Fig. 7. Voltage and temperature response (Subfigure A) and absolute value of the voltage and temperature error (Subfigure B) for the Mixed-3 validation profile. Lithium-ion cell: LG Chem INR18650HG2.
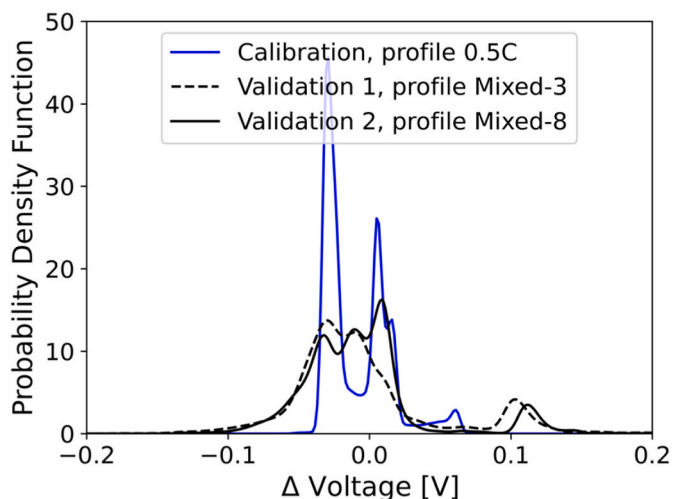

Fig. 8. Probability density function of the voltage error for the calibration and validation curves. Lithium-ion cell: LG Chem INR18650HG2.

Table 2
Optimum operational and constructive parameters obtained in the calibration procedure of the cell LGHG2 using dynamic current profiles.

Parameter	Symbol	Units	Value
Cathode thickness	t_{cat}	μm	55.52
Anode thickness	t_{an}	μm	68.00
Separator thickness	t_{sep}	μm	17.46
Cathode first charge capacity	q_{fcc}^{cat}	mAh/g	197.68
Anode first charge capacity	q_{fcc}^{an}	mAh/g	365.86
Cathode first discharge capacity	q_{fdc}^{cat}	mAh/g	180.84
Anode first discharge capacity	q_{fdc}^{an}	mAh/g	357.61
Particle size of the cathode material	R_{cat}	μm	0.05
Particle size of the anode material	R_{an}	μm	15.61
Contact resistance	R_c	$\Omega \cdot m^2$	$3.96 \cdot 10^{-4}$
Anode capacity	C_{an}	Ah	3.16
Cathode capacity	C_{cat}	Ah	3.05

similar reported values; the calibration processes have been performed for the same cell, but the current profiles used in each case differ. Most of the constructive parameters and loading factors have remained almost identical, but the most remarkable difference is observed in the cathode particle size, which is vital to capturing the cell's dynamic behavior, especially in the low-SOC region.
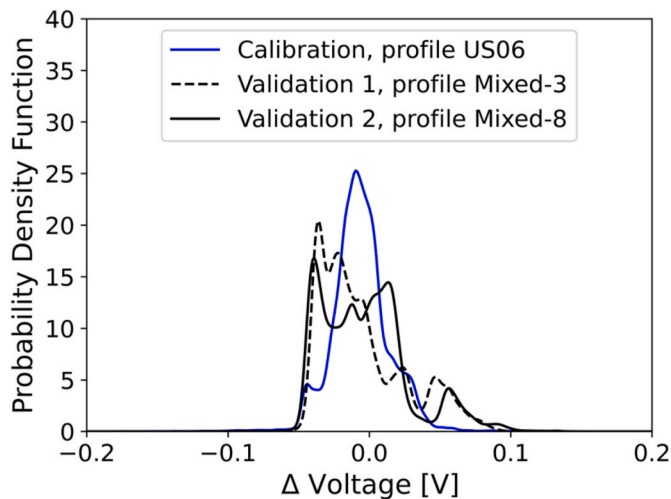
Fig. 9 compares the voltage response characterized experimentally with the one predicted by the electrochemical model (Subfigure A) for the dynamic calibration profile US06. Again, the solution depicted is the one that minimizes the overall error objective function, so it includes the optimized performance and constructive parameters. As can be observed, the model prediction is well-fitted to the results of the experimental tests. In terms of global goodness of fit indicators, the $RMSE_V$ is 0.0220 V and the 95th percentile of the voltage error is 0.0424 V. With this procedure, no remarkable differences in terms of accuracy
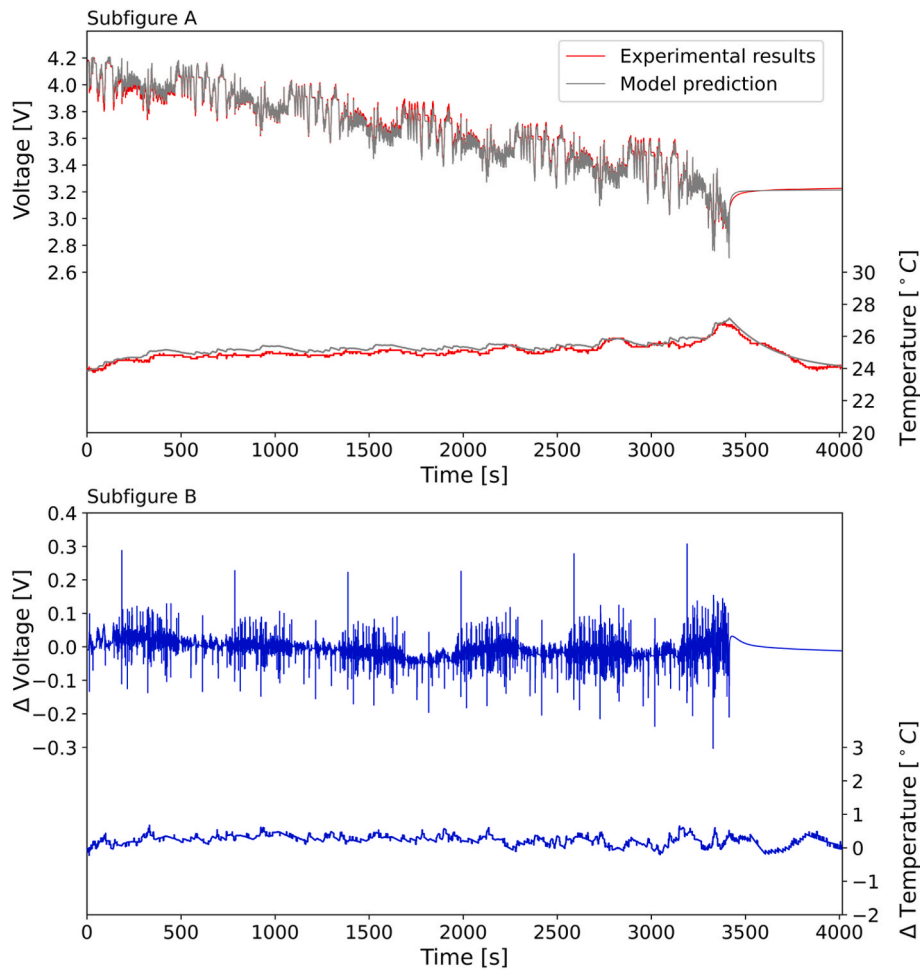
Fig. 9. Simulated and experimental voltage response (Subfigure A) and absolute value of the voltage error (Subfigure B) for the US06 calibration profile. Lithium-ion cell: LG Chem INR18650HG2.

Fig. 10. Comparison of the probability density function of the voltage error for the calibrated and validated profiles. Lithium-ion cell: LG Chem INR18650HG2.

Table 3
Optimum operational and constructive parameters obtained in the calibration procedure of the cell Panasonic 18650 PF using dynamic current profiles.

Parameter	Symbol	Units	Value
Cathode thickness	t_{cat}	μm	70.67
Anode thickness	t_{an}	μm	82.12
Separator thickness	t_{sep}	μm	11.71
Cathode first charge capacity	q_{fcc}^{cat}	mAh/g	207.14
Anode first charge capacity	q_{fcc}^{an}	mAh/g	393.10
Cathode first discharge capacity	q_{fdc}^{cat}	mAh/g	191.81
Anode first discharge capacity	q_{fdc}^{an}	mAh/g	347.97
Particle size of the cathode material	R_{cat}	μm	11.81
Particle size of the anode material	R_{an}	μm	9.93
Contact resistance	R_c	Ω·m²	6.28 10⁻⁴
Anode capacity	C_{an}	Ah	4.04
Cathode capacity	C_{cat}	Ah	3.36

during the calibration are found in comparison to the calibration with constant C-rate curves.

The satisfactory results in the calibration fitting process are also corroborated when analyzing the total energy charged and discharged during the cycle. The relative discrepancy between the experimental and simulated results, $\varepsilon_{ch} = -0.31\%$ and $\varepsilon_{dch} = -0.15\%$ is relatively low.

The histogram plot of Fig. 10 is helpful in gaining more insights into the error distribution and serves as an overall descriptor of the error achieved in the calibration and validation processes. It confirms the trend observed in Fig. 9 (Subfigure B): the calibration curve can be fitted with good precision, and the error is mainly concentrated in the range $[-0.05, 0.05]$ V. In both validation profiles, the error is grouped within the range $[-0.1\ V, +0.1\ V]$. The RMSE and the 95th percentile of error of the Mixed-3 Profile ($RMSE_V = 0.0315$ V, $\Delta V_{95th} = 0.0577\ V$) and the Mixed-8 profile ($RMSE_V = 0.0315$ V, $\Delta V_{95th} = 0.0612\ V$) confirms that
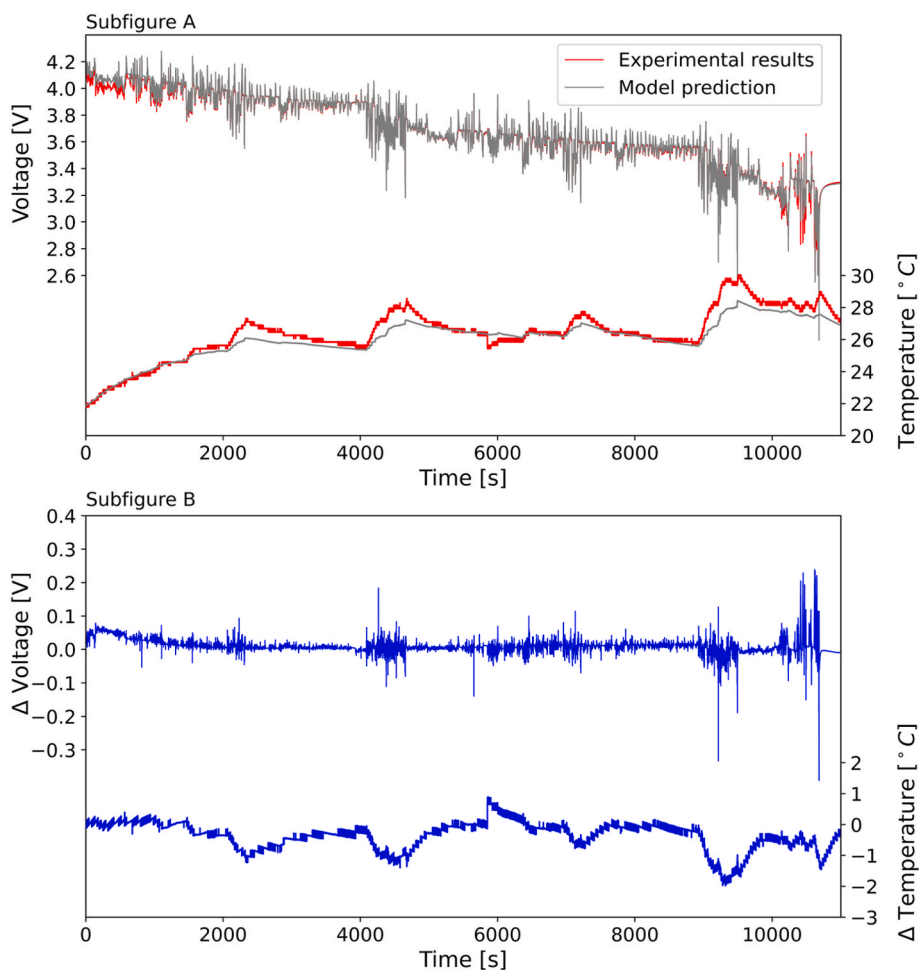
Fig. 11. Voltage and temperature response (Subfigure A) and absolute value of the voltage and temperature error (Subfigure B) for the Cycle-1 calibration profile. Lithium-ion cell: Panasonic 18650 PF.
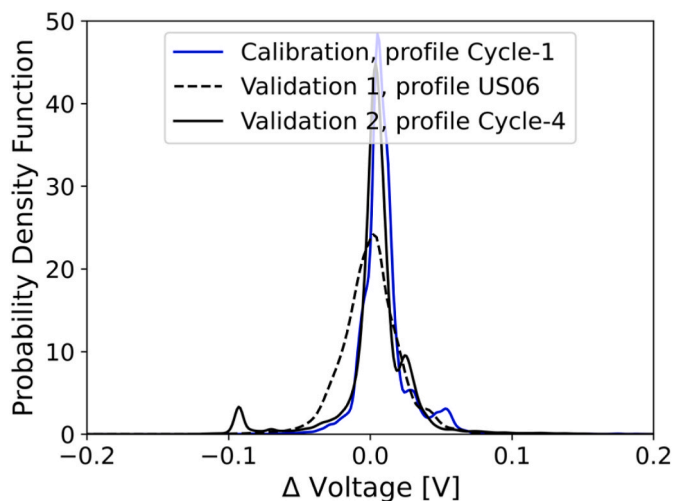

Fig. 12. Comparison of the probability density function of the voltage error for the calibrated and validated profiles. Lithium-ion cell: Panasonic 18650 PF.

the error is very small. Again, the deviation in temperature is very low, being the maximum discrepancy between the experimental and numerical results of 0.7 °C.

Fig. 10 shows how in this case, the overall error on the performance test curves has been better distributed and not concentrated towards low SOC conditions, with a better interpretation of the global cell performance. As can be observed in Fig. 10, the prevalence of error at +0.1 V identified in Fig. 8 no longer appears.

Everything points towards a significant improvement in the fitting capabilities when using a single dynamic test to calibrate the cell model. With a single test, a broader and more continuous spectrum of operating conditions is provided to the optimizer, rather than a very scarce and discrete set of operating conditions, like the ones used for constant current tests, and this significantly improves the accuracy when considering dynamic scenarios. Of course, the accuracy of the constant C-rate fitting methodology can be improved by providing a more extensive dataset, but this would be more time-consuming in terms of both experimental efforts and computing costs.

The alternative methodology of calibrating and validating the cell with dynamic profiles has improved the accuracy moderately and has an acceptable computing cost. It takes about 50 h to find the optimum constructive and operational parameters in the calibration stage, but it shows a strong dependence on the experimental test duration. The resolution time of each validation profile is about 10 min. The calculations have been performed using 1 core of a workstation equipped with an Intel Xeon Silver 4214R (2.4 GHz).

Given the benefits mentioned above in terms of precision, calibrating and validating the cell with dynamic current profiles has also been adopted to evaluate the other cell specimen with different cathode chemistry.

Table 4
Summary of the main goodness of fit indicators for all the calibration and validation profiles for the cells subject to analysis.

Test profile	Type	Cell	ε_{ch} [%]	ε_{dch} [%]	$RMSE_V$ [V]	ΔV_{95th} [V]	$RMSE_T$ [°C]
OCV	Calibration (Constant C-rate)	LG Chem INR18650HG2 (NMC811)	–	−0.21	0.0367	0.0884	0.09
0.5C	Calibration (Constant C-rate)	LG Chem INR18650HG2 (NMC811)	–	−0.25	0.0247	0.0377	0.14
2C	Calibration (Constant C-rate)	LG Chem INR18650HG2 (NMC811)	–	−0.49	0.0319	0.0631	0.63
Mixed-3	Validation (Dynamic)	LG Chem INR18650HG2 (NMC811)	1.14	−1.22	0.0531	0.1107	0.34
Mixed-8	Validation (Dynamic)	LG Chem INR18650HG2 (NMC811)	0.62	−0.99	0.0463	0.1124	0.28
US06	Calibration (Dynamic)	LG Chem INR18650HG2 (NMC811)	−0.31	−0.15	0.0220	0.0424	0.27
Mixed-3	Validation (Dynamic)	LG Chem INR18650HG2 (NMC811)	−0.24	−0.13	0.0315	0.0577	0.15
Mixed-8	Validation (Dynamic)	LG Chem INR18650HG2 (NMC811)	−0.35	−0.08	0.0315	0.0612	0.17
Cycle-1	Calibration (Dynamic)	Panasonic 18650 PF (NCA)	0.42	0.11	0.0217	0.0474	0.57
US06	Validation (Dynamic)	Panasonic 18650 PF (NCA)	0.49	−0.44	0.0357	0.0438	0.61
Cycle-4	Validation (Dynamic)	Panasonic 18650 PF (NCA)	0.22	0.14	0.0281	0.0707	0.66

4.2.2. Cell 2: panasonic 18650 PF

The robustness and validity of the model while predicting the response of other cell chemistries have been evaluated by reproducing the same procedure for the cell Panasonic 18650 PF (NCA). Table 3 collects the optimum performance and constructive parameters, and Fig. 11 represents the fitting of the electrochemical model to the experimental calibration curve (Cycle-1). The goodness of fit indicators of the calibration curve ($RMSE_V = 0.0217$ V, $\Delta V_{95th} = 0.0474$ V, $\varepsilon_{ch} = 0.42\%$, $\varepsilon_{dch} = 0.11\%$) verify the proper fitting. Again, all the discrepancies are contained in the interval $[-0.1$ V, $+0.1$ V]. The fitting to the validation profiles is also of good quality, as illustrated in Fig. 12 and confirmed in the error analysis of the US06 profile ($RMSE_V = 0.0357$ V, $\Delta V_{95th} = 0.0438$ V), and Cycle-4 $RMSE_V = 0.0281$ V, $\Delta V_{95th} = 0.0707$ V). Regarding the temperature difference, maximum deviations are not exceeding 2.0 °C. Hence, the calibration and validation procedure respond satisfactorily while modeling other cathode chemistries (NCA).

4.3. Performance summary

Table 4 summarizes the main goodness of fit indicators for the different calibration procedures and subsequent validations for the different chemistries subject to analysis.

Both methodologies applied on the cell LG Chem INR18650HG2 (NMC811) are shown: (i) calibration using three constant current performance tests and (ii) calibration using a single dynamic cycle. Oppositely, for the Panasonic 18650 PF cell, only the calibration based on the dynamic signals has been performed.

The indicators included in the table correspond with the relative error in total energy charged and discharged from the cell, the Root Mean Square Error (RMSE) on voltage and temperature, and the 95th percentile of error fit well between experimental and simulated outputs.

5. Conclusions

In the present research work, a novel methodology for calibrating and validating an electrochemical lithium-ion cell model at a reference temperature of 25 °C has been proposed. The model fits operational and constructive parameters of the cell that are a priori unknown to the end-users but have a decisive influence on its dynamic response. The fitting is conducted automatically using a genetic algorithm and setting an objective function. The main conclusions of the research are listed below:

- The set of 14 constructive parameters and physical properties of the cell materials selected for the analysis allows for precise fitting for the chemistries subject to analysis (NMC 811 and NCA) with a reasonable computational cost.
- Calibrating the model with three constant current tests provides a satisfactory fitting of the voltage and temperature curves. Deviations in voltage found during the validation process are contained in the

range of [-0.1 V, +0.15 V] for the NMC 811 cell. The fitting error tends to concentrate on the low SOC region, and the maximum RMSE of the validation curves is 0.0531 V.
- A better fitting during the validation stage is achieved if the electrochemical model is calibrated with a dynamic high-rate profile rather than constant C-rate curves. With this approach, the maximum RMSE for the voltage profiles used to validate the model is 0.0315 V for the NMC 811 cell and 0.0357 V for the NCA cell. In all the calibration and validation profiles, the probability density function demonstrates that the discrepancies between the model and the experimental results are within the range [-0.1 V, +0.1 V].
- Given that the working temperature range considered for this study has been within nominal values very similar to the ambient temperature, no secondary effects driven by degradation mechanisms have occurred, and the parameters selected for considering temperature effects on the calibration methodology have captured the tendencies with outstanding fidelity for all cases, yielding a maximum global deviation of RMSE of 0.66 °C.

The current work establishes a robust and reliable method to calibrate cell models under controlled and stable operations under a constant ambient temperature. Nonetheless, extreme operating conditions like fast charging, high power demands with C-rates above 10, or working conditions where the ambient temperature can be either extremely low or extremely high can significantly affect how the reactions inherent to the working principle of lithium-ion batteries are hindered or accelerated.

In future research, the model will be extended to make reliable predictions with low and high-temperature effects that some authors have linked to changes in the physical properties of the materials related to how internal resistance changes. Other models like mechanical stress prediction models will be evaluated to state their relevance for said studies.

Author statement

Antonio García: Conceptualization and Methodology; **Javier Monsalve-Serrano**: Validation and Investigation and Writing - Review & Editing; **Alberto Ponce-Mora Villalta**: Investigation and Writing - original draft; **Álvaro Fogué-Robles**: Formal analysis and Writing - original draft.

Declaration of competing interest

The authors declare that they have no known competing financial interests or personal relationships that could have appeared to influence the work reported in this paper.

Data availability

The authors do not have permission to share data.

Acknowledgments

References

[1] European vehicle emissions standards – euro 7 for cars, vans, lorries and buses. Eur Com n.d. https://ec.europa.eu/info/law/better-regulation/have-your-say/initiatives/12313-European-vehicle-emissions-standards-Euro-7-for-cars-vans-lorries-and-buses_en.

[2] LCTPi. Low-Carbon Transport fuels 2022;1–7.

[3] Samsun RC, Antoni L, Rex M, Stolten D. Deployment status of fuel cells in road transport : 2021 update, vol. 542; 2021.

[4] IEA. The Future of Hydrogen: seizing today's opportunities. 2019.

[5] Kim GH, Pesaran A, Spotnitz R. A three-dimensional thermal abuse model for lithium-ion cells. J Power Sources 2007;170:476–89. https://doi.org/10.1016/j.jpowsour.2007.04.018.

[6] International Energy Agency. Global EV Outlook 2021 - accelerating ambitions despite the pandemic. 2021.

[7] Bell L, Spinler S, Winkenbach M. Economic, social and ecological impact assessment of mixed light rail, battery-electric vehicles, fuel cell-electric vehicles and electrified cargo bikes in urban environment of advanced integrated simulation approach. SSRN Electron J 2022;43:2086–107. https://doi.org/10.2139/ssrn.4011273.

[8] Sanguesa JA, Torres-Sanz V, Garrido P, Martinez FJ, Marquez-Barja JM. A Review on electric vehicles: technologies and challenges. Smart Cities 2021;4:372–404. https://doi.org/10.3390/smartcities4010022.

[9] Kim HJ, Krishna TNV, Zeb K, Rajangam V, Muralee Gopi CVV, Sambasivam S, et al. A comprehensive review of li-ion battery materials and their recycling techniques, vol. 9; 2020. https://doi.org/10.3390/electronics9071161.

[10] Löbberding H, Wessel S, Offermanns C, Kehrer M, Rother J, Heimes H, et al. From cell to battery system in BEVs: analysis of system packing efficiency and cell types. World Electr Veh J 2020;11:77. https://doi.org/10.3390/wevj11040077.

[11] Li C, Yang W, He W, Zhang X, Zhu J. Multifunctional surfactants for synthesizing high-performance energy storage materials. Energy Storage Mater 2021;43:1–19. https://doi.org/10.1016/j.ensm.2021.08.033.

[12] Miao Y, Hynan P, Von Jouanne A, Yokochi A. Current li-ion battery technologies in electric vehicles and opportunities for advancements. Energies 2019;12:1–20. https://doi.org/10.3390/en12061074.

[13] Ukaew A. Model based system design for electric vehicle conversion. New Trends Electr. Veh. Powertrains, IntechOpen; 2019. https://doi.org/10.5772/intechopen.77265.

[14] Semeraro C, Caggiano M, Olabi A-G, Dassisti M. Battery monitoring and prognostics optimization techniques: challenges and opportunities. Energy 2022;255:124538. https://doi.org/10.1016/j.energy.2022.124538.

[15] Edge JS, O'Kane S, Prosser R, Kirkaldy ND, Patel AN, Hales A, et al. Lithium ion battery degradation: what you need to know. Phys Chem Chem Phys 2021;23:8200–21. https://doi.org/10.1039/d1cp00359c.

[16] Lai X, Zheng Y, Sun T. A comparative study of different equivalent circuit models for estimating state-of-charge of lithium-ion batteries. Electrochim Acta 2018;259:566–77. https://doi.org/10.1016/j.electacta.2017.10.153.

[17] Wen J, Chen X, Li X, Li Y. SOH prediction of lithium battery based on IC curve feature and BP neural network. Energy 2022;261:125234. https://doi.org/10.1016/j.energy.2022.125234.

[18] Zhou Y, Dong G, Tan Q, Han X, Chen C, Wei J. State of health estimation for lithium-ion batteries using geometric impedance spectrum features and recurrent Gaussian process regression. Energy 2023;262:125514. https://doi.org/10.1016/j.energy.2022.125514.

[19] Cui Z, Kang L, Li L, Wang L, Wang K. A combined state-of-charge estimation method for lithium-ion battery using an improved BGRU network and UKF. Energy 2022;259:124933. https://doi.org/10.1016/j.energy.2022.124933.

[20] Falconi A. Electrochemical modeling of lithium-ion cell behaviour for electric vehicles to cite this version : HAL Id : tel-01730759 Modélisation électrochimique du comportement d ' une cellule Li-ion pour application au véhicule électrique. 2018.

[21] Jiang W, Zhou Q, Lu F, Chen Y, Ma Z. A thermal-electrochemical-mechanical coupled model based on non-equilibrium thermodynamics of Li-ion batteries. J Energy Storage 2022;55:105655. https://doi.org/10.1016/j.est.2022.105655.

[22] Duan X, Jiang W, Zou Y, Lei W, Ma Z. A coupled electrochemical–thermal–mechanical model for spiral-wound Li-ion batteries. J Mater Sci 2018;53:10987–1001. https://doi.org/10.1007/s10853-018-2365-6.

[23] Wang X, Liu S, Zhang Y, Lv S, Ni H, Deng Y, et al. A Review of the power battery thermal management system with different cooling, heating and coupling system. Energies 2022;15:1963. https://doi.org/10.3390/en15061963.

[24] Drummond R, Bizeray AM, Howey DA, Duncan SR. A feedback interpretation of the doyle-fuller-newman lithium-ion battery model. IEEE Trans Control Syst Technol 2020;28:1284–95. https://doi.org/10.1109/TCST.2019.2909722.

[25] Brodsky P, Canova M, Kim JH, Ramesh P, Bae C, Deng J, et al. Calibration of electrochemical models for Li-ion battery cells using three-electrode testing. SAE Tech Pap 2020;2020-April:1–14. https://doi.org/10.4271/2020-01-1184.

[26] Masoudi R, Uchida T, McPhee J. Parameter estimation of an electrochemistry-based lithium-ion battery model. J Power Sources 2015;291:215–24. https://doi.org/10.1016/j.jpowsour.2015.04.154.

[27] Santhanagopalan S, White RE. Online estimation of the state of charge of a lithium ion cell. J Power Sources 2006;161:1346–55. https://doi.org/10.1016/j.jpowsour.2006.04.146.

[28] Tagade P, Hariharan KS, Basu S, Verma MKS, Kolake SM, Song T, et al. Bayesian calibration for electrochemical thermal model of lithium-ion cells. J Power Sources 2016;320:296–309. https://doi.org/10.1016/j.jpowsour.2016.04.106.

[29] Rahman MA, Anwar S, Izadian A. Electrochemical model parameter identification of a lithium-ion battery using particle swarm optimization method. J Power Sources 2016;307:86–97. https://doi.org/10.1016/j.jpowsour.2015.12.083.

[30] Forman JC, Moura SJ, Stein JL, Fathy HK. Genetic identification and Fisher identifiability analysis of the Doyle-Fuller-Newman model from experimental cycling of a LiFePO 4 cell. J Power Sources 2012;210:263–75. https://doi.org/10.1016/j.jpowsour.2012.03.009.

[31] Zhang L, Wang L, Hinds G, Lyu C, Zheng J, Li J. Multi-objective optimization of lithium-ion battery model using genetic algorithm approach. J Power Sources 2014;270:367–78. https://doi.org/10.1016/j.jpowsour.2014.07.110.

[32] Marcicki J, Canova M, Conlisk AT, Rizzoni G. Design and parametrization analysis of a reduced-order electrochemical model of graphite/LiFePO4 cells for SOC/SOH estimation. J Power Sources 2013;237:310–24. https://doi.org/10.1016/j.jpowsour.2012.12.120.

[33] Ramadesigan V, Chen K, Burns NA, Boovaragavan V, Braatz RD, Subramanian VR. Parameter estimation and capacity fade analysis of lithium-ion batteries using reformulated models. J Electrochem Soc 2011;158:A1048. https://doi.org/10.1149/1.3609926.

[34] Kim M, Chun H, Kim J, Kim K, Yu J, Kim T, et al. Data-efficient parameter identification of electrochemical lithium-ion battery model using deep Bayesian harmony search. Appl Energy 2019;254:113644. https://doi.org/10.1016/j.apenergy.2019.113644.

[35] Chu Z, Jobman R, Rodríguez A, Plett GL, Trimboli MS, Feng X, et al. A control-oriented electrochemical model for lithium-ion battery. Part II: parameter identification based on reference electrode. J Energy Storage 2020;27:101101. https://doi.org/10.1016/j.est.2019.101101.

[36] Fan G. Systematic parameter identification of a control-oriented electrochemical battery model and its application for state of charge estimation at various operating conditions. J Power Sources 2020;470:228153. https://doi.org/10.1016/j.jpowsour.2020.228153.

[37] Gamma Technologies. GT-AutoLion. Thermal battery performance and aging simulation. 2022.

[38] Legrand N, Raël S, Knosp B, Hinaje M, Desprez P, Lapicque F. Including double-layer capacitance in lithium-ion battery mathematical models. J Power Sources 2014;251:370–8. https://doi.org/10.1016/j.jpowsour.2013.11.044.

[39] Newman J, Tiedemann W. Porous-electrode theory with battery applications. AIChE J 1975;21:25–41. https://doi.org/10.1002/aic.690210103.

[40] Salvadori A, Grazioli D, Geers MGD. Governing equations for a two-scale analysis of Li-ion battery cells. Int J Solid Struct 2015;59:90–109. https://doi.org/10.1016/j.ijsolstr.2015.01.014.

[41] Tjaden B, Cooper SJ, Brett DJ, Kramer D, Shearing PR. On the origin and application of the Bruggeman correlation for analysing transport phenomena in electrochemical systems. Curr Opin Chem Eng 2016;12:44–51. https://doi.org/10.1016/j.coche.2016.02.006.

[42] Chung DW, Ebner M, Ely DR, Wood V, Edwin García R. Validity of the Bruggeman relation for porous electrodes. Model Simulat Mater Sci Eng 2013;21. https://doi.org/10.1088/0965-0393/21/7/074009.

[43] Vadakkepatt A, Trembacki B, Mathur SR, Murthy JY. Bruggeman's exponents for effective thermal conductivity of lithium-ion battery electrodes. J Electrochem Soc 2016;163:A119–30. https://doi.org/10.1149/2.0151602jes.

[44] Newman J, Thomas-Aleya KE. Electrochemical systems. third ed. Wiley-Interscience; 2004.

[45] Terrani KA. Model based optimal control, estimation, and validation of lithium-ion batteries, vol. 67. DNA Mediat Assem Protein Heterodimers Membr Surfaces; 2016.

[46] Xia L, Najafi E, Bergveld HJ, Donkers MCF. A computationally efficient implementation of an electrochemistry-based model for lithium-ion batteries. IFAC-PapersOnLine 2017;50:2169–74. https://doi.org/10.1016/j.ifacol.2017.08.276.

[47] Dickinson EJF, Wain AJ. The Butler-Volmer equation in electrochemical theory: origins, value, and practical application. J Electroanal Chem 2020;872:114145. https://doi.org/10.1016/j.jelechem.2020.114145.

[48] Hess A, Roode-Gutzmer Q, Heubner C, Schneider M, Michaelis A, Bobeth M, et al. Determination of state of charge-dependent asymmetric Butler-Volmer kinetics for LixCoO2 electrode using GITT measurements. J Power Sources 2015;299:156–61. https://doi.org/10.1016/j.jpowsour.2015.07.080.

[49] Guidelli R, Compton RG, Feliu JM, Gileadi E, Lipkowski J, Schmickler W, et al. Defining the transfer coefficient in electrochemistry: an assessment (IUPAC Technical Report). Pure Appl Chem 2014;86:245–58. https://doi.org/10.1515/pac-2014-5026.

[50] Jindal P, Katiyar R, Bhattacharya J. Evaluation of accuracy for Bernardi equation in estimating heat generation rate for continuous and pulse-discharge protocols in

LFP and NMC based Li-ion batteries. Appl Therm Eng 2022;201:117794. https://doi.org/10.1016/j.applthermaleng.2021.117794.

[51] Bizeray AM, Zhao S, Duncan SR, Howey DA. Lithium-ion battery thermal-electrochemical model-based state estimation using orthogonal collocation and a modified extended Kalman filter. J Power Sources 2015;296:400–12. https://doi.org/10.1016/j.jpowsour.2015.07.019.

[52] Kollmeyer P, Vidal C, Naguib M, Skells MLG. 18650HG2 Li-ion battery data and example deep neural network xEV SOC estimator script. Mendeley Data 2020;V3. https://doi.org/10.17632/cp3473x7xv.3.

[53] Kollmeyer P. Panasonic 18650PF Li-ion battery data. Mendeley Data 2018;V1. https://doi.org/10.17632/wykht8y7tg.1.

[54] Pan Y, Kong X, Yuan Y, Sun Y, Han X, Yang H, et al. Detecting the foreign matter defect in lithium-ion batteries based on battery pilot manufacturing line data analyses. Energy 2023;262:125502. https://doi.org/10.1016/j.energy.2022.125502.

[55] Astaneh M, Andric J, Löfdahl L, Maggiolo D, Stopp P, Moghaddam M, et al. Calibration optimization methodology for lithium-ion battery pack model for electric vehicles in mining applications. Energies 2020;13. https://doi.org/10.3390/en13143532.

Notation

Abbreviatures

BEV: Battery Electric Vehicle
CO2: Carbon dioxide
C-rate: current level relative to total capacity
DFN: Doyle-Fuller-Newman
ECM: Equivalent Circuit Model
EUVI: EURO VI legislation
FCC: First Charge Capacity
FDC: First Discharge Capacity
GA: Genetic Algorithms
GN: Gauss-Newton method
HPPC: Hybrid Power Pulse Characterization
ICE: Internal Combustion Engine
LCO: Lithium Cobalt Oxide
LFP: Lithium–Iron-Phosphate oxide
LM: Levenberg-Marquardt method
NCA: Lithium Nickel–Cobalt–Aluminum oxide
NCM: Lithium Nickel–Cobalt–Manganese oxide
NOx: Nitrogen Oxides
OCV: Open Circuit Voltage
ODE: Ordinary Differential Equation
PSO: Particle Swarm Optimization
RMSE: Root Mean Square Error
SEI: Solid Electrolyte Interface
SOC: State of Charge
SOH: State of Health
TRL:: Technology Readiness Levels

Symbols

Symbol: Description
a_{dl}: Volume specific interfacial area for double-layer capacitance effect
a_s: Volume specific reaction surface area
A_c: Total cell external area
A_s: Area of contact between solid phase and current collector
c_e: Molar concentration of lithium ions in the electrolyte
c_p: Specific heat capacity
c_s: Molar concentration of lithium in the solid phase
C: Specific capacitance
C_s: Capacity of the cell

$C_{s,max}$: Theoretical capacity
D_e: Electrolyte diffusion coefficient
D_e^{eff}: Electrolyte effective diffusion coefficient
D_s: Diffusion coefficient of lithium in the solid phase
E_{ch}: Total energy input during charge
E_{dch}: Total energy output during discharge
E_{ov}: Objective function based on weighted overall error
E_T: Temperature term of the overall error function
E_V: Voltage term of the overall error function
$f_{\pm}$: Molar activity coefficient in the electrolyte
F: Faraday's constant
h: Convective heat transfer coefficient
i_0: Exchange current density
I: External electric current
I_{ch}: Electric current during charging operation mode
I_{dch}: Electric current during discharging operation mode
j^{tc}: Total internal current
j^{Li}: Reaction current of lithium
k^{eff}: Electrolyte effective ionic conductivity
k_D^{eff}: Electrolyte effective ionic diffusional conductivity
L: Total layer longitudinal thickness
p: Bruggeman tortuosity exponent factor
q_{fcc}^{cat}: Mass-specific first charge capacity
q_{fdc}^{cat}: Mass-specific first discharge capacity
q_{th}^{cat}: Mass-specific theoretical capacity
$\dot{q}_{conv}$: Convective heat flow
$\dot{q}_{gen}$: Total heat flow generated during cell operation
$\dot{q}_{ohm}$: Heat rate generated through internal ohm effect
$\dot{q}_{rev}$: Heat rate generated through reversible processes
$\dot{q}_{rxn}$: Heat rate generated through redox reactions
r: Radial dimension
R^0: Gas constant
R_c: Contact resistance
R_{SEI}: SEI resistive film layer
R_u: Universal gas constant
t: Time
t_+^0: Transference number
T: Temperature
T_{amb}: Ambient Temperature
U: Open circuit potential
V_c: Cell volume
V_{ch}: Voltage during charging operation mode
V_{dch}: Voltage during discharging operation mode
V_{exp}: Voltage from experimental measurement
V_{sim}: Voltage predicted in the simulation
w_T: Weight factor for temperature term on the objective function
w_V: Weight factor for voltage term on the objective function
x: Longitudinal dimension
α_a: Anode charge transfer coefficient
α_c: Cathode charge transfer coefficient
γ_{fcc}^{cat}: Ratio of first charge capacity
γ_{fdc}^{cat}: Ratio of first discharge capacity
ε: Electrolyte porosity
ε_{ch}: Relative error in charged energy between simulation and experiment
ε_{dch}: Relative error in discharged energy between simulation and experiment
ΔE_{ch}: Absolute error in charged energy between simulation and experiment
ΔE_{dch}: Absolute error in discharged energy between simulation and experiment
η: Over potential
ρ: Cell density
σ_s^{eff}: Effective electric conductivity of solid phase
φ_e: Electrolyte potential
φ_s: Solid phase potential